Journal of Earth Science, *Vol. 31*, *No. 2*, *p. 271–286*, *April 2020* *ISSN 1674-487X*
Printed in China
https://doi.org/10.1007/s12583-019-1273-2

Factors Controlling Deposition of Metallic Minerals in the Meng'entaolegai Ag-Pb-Zn Deposit, Inner Mongolia, China: Evidence from Fluid Inclusions, Isotope Systematics, and Thermodynamic Model

He Yang, **Wanli Ma**, **Rui Wang**, **Xueli Ma**, **Keyong Wang***
College of Earth Sciences, *Jilin University*, *Changchun* 130061, *China*
He Yang: https://orcid.org/0000-0002-0786-0682; Keyong Wang: https://orcid.org/0000-0002-7764-2074

ABSTRACT: The Meng'entaolegai Ag-Pb-Zn vein-type deposit in Inner Mongolia, NE China is hosted in biotite/muscovite granite. This deposit includes the western (Zn-rich, deepest), middle (Zn-Pb rich) and eastern (Pb-Ag-rich, shallowest) ore-blocks. To better understand the metallogenic processes in ore district, we have undertaken a series of studies including fluid inclusion microthermometry, H-O-S-Pb isotope compositions and thermodynamic modeling. Based on fluid inclusion petrography, microthermometry results and H-O isotope compositions, the ore-forming H_2O-NaCl fluid inclusions are characterized by medium temperature and medium salinity. And two kinds of fluid processes (boiling in western and middle ore-block and fluid mixing in the eastern ore-block) were identified to explain the ore fluid evolution. More importantly, log f_{O_2}-pH diagrams of $\delta^{34}S$ contours with the stability fields of Fe- and Cu-, Zn-, Pb-, and Ag-bearing minerals were constructed to restore the physicochemical conditions of ore-forming fluid in the western (270 °C and 80 bars), middle (250 °C and 70 bars), and eastern (230 °C and 50 bars) ore-blocks. As a result, the ore-forming conditions in the western and middle ore-block were similar. In the eastern ore-block, the fluids may have changed from acidic, S-poor and $\delta^{34}S(\Sigma S)\approx 2.8$ to neutral, S-richer and $\delta^{34}S(\Sigma S)\approx 0.5$, which imply that neutral S-rich meteoric water was mixed with the magmatic fluid. Meanwhile, the activity of Ag+ was estimated to be about 10 ppm–9 ppm in the middle ore-block, but in the eastern ore-block it was about ~10 ppm–12 ppm. We proposed that the key for Ag ore deposition was likely to be neutralization led by fluid mixing.
KEY WORDS: fluid inclusions, isotope systematics, thermodynamic model, Ag-Pb-Zn deposit, Meng'entalegai, NE China.

0 INTRODUCTION

The Great Hinggan Range (GHR) is one of the most important nonferrous ore belts in northeastern (NE) China. The GHR hosts a number of porphyry Mo-(Cu), skarn Fe-(Sn), epithermal Au-Ag, and vein-type Ag-Pb-Zn deposits (Shu et al., 2016, 2013; Zhai et al., 2015, 2014a, b, c, 2013; Zhai and Liu, 2014; Wu et al., 2011a, b; Zeng et al., 2011, 2009). Ag-Pb-Zn vein deposits are particularly common in the southern GHR segment, including the Meng'entaolegai, Shuangjianzishan, Bianjiadayuan, and Bairendaba-Weilasituo deposits (Zhai et al., 2018; Liu C H et al., 2016; Liu Y F et al., 2016; Ruan et al., 2015; Ouyang et al., 2014; Zhang et al., 2006; Zhu et al., 2006). Geological characteristics of these deposits were shown in Table 1.

Silver-lead-zinc (Ag-Pb-Zn) vein-type deposits are clearly hydrothermal in origin, although the source of ore-forming fluids and metals may be magmatic and/or nonmagmatic (Li et al., 2019; Kissin and Mango, 2014). In the description of the types of Ag-Pb-Zn vein-type deposits, two major types are recognized: (a) mesothermal hydrothermal vein deposit; (b) epithermal deposits. Ag-Pb-Zn vein deposits (e.g., Shuangjianzishan, Bianjiadayuan et al.) in southern GHR segment form at medium temperatures (200–350 °C) or lack typical alteration zones (Zhai et al., 2018; Liu C H et al., 2016; Liu Y F et al., 2016; Ruan et al., 2015; Ouyang et al., 2014), generally considered as mesothermal hydrothermal vein deposit. However, in many cases, fluid (metal) sources and the factors controlling the deposition of Ag are still controversial of unknown.

Unlike other Ag-Pb-Zn deposits in the region, the Meng'entaolegai Ag-Pb-Zn deposit is hosted in muscovite/biotite granite and with no direct contact with sedimentary rocks. The well-preserved vein deposit allows for a systematic investigation of fluid origin and deposition mechanisms. Previous studies on the Meng'entaolegai deposit have addressed ore deposit geology (Zhang et al., 2006; Zhu et al., 2006); whole rock geochemistry and geochronology of intrusive rocks (Jiang et al., 2011); geochronology (Jiang et al., 2011); stable isotope (S, H, O), Pb isotope geochemistry (Zhu et al., 2006); trace element

*Corresponding author: wangky@jlu.edu.cn

Manuscript received November 29, 2018.
Manuscript accepted September 30, 2019.

geochemistry of minerals (Zhang et al., 2006). These workers group the orebodies into the western (Zn-rich, deepest), middle (Zn-Pb rich) and eastern (Pb-Ag-rich, shallowest) ore-blocks (Zhang et al., 2006; Zhu et al., 2006). However, no studies were conducted to reveal the nature and evolution of ore-forming fluids and explain the different mineralization styles in these three ore-blocks.

This study aims to solve the following questions: what kind of fluids had caused the different mineralization styles in these three ore-blocks, e.g., why economic Ag mineralization occurs mainly in the eastern ore-block. We also aim to constrain the fluid evolution history. In this contribution, we report the results of fluid inclusion and multiple-isotope analyses and thermodynamic modeling. We discuss the physicochemical conditions of ore-forming fluid system.

1 GEOLOGICAL SETTING

The Meng'entaolegai deposit is situated in the southern GHR section (Figs. 1b, 1c) in NE China, which lies in the eastern part of the Central Asian orogenic belt (CAOB) (Fig. 1a). The CAOB is widely accepted to be evolved through complex terrane accretions and closure of the Paleo-Asian and Mongol-Okhotsk Oceans from the Neoproterozoic to the Late Mesozoic (Wilde and Zhou, 2015), and represents the world's largest Phanerozoic orogenic belt (Jahn, 2004).

In the southern GHR segment, Ag-Pb-Zn deposits are mostly related to Jurassic to Cretaceous magmatism (Zhai et al., 2018, 2014b, 2013; Chen et al., 2007; Mao et al., 2005; Zhao and Zhang, 1997). At the Meng'entaolegai deposit, Mesoproterozoic schist and gneiss were locally exposed in the western part of the district, and was unconformably overlain by Permian sandstone-shale-limestone and Jurassic clastic and volcanic rocks. Permian and Jurassic rocks are not metamorphosed. The Duerji granites were emplaced in the eastern part of the district, and Triassic granites are the ore host in the middle part of the district.

2 ORE DEPOSIT GEOLOGY

The Meng'entaolegai Ag-Pb-Zn polymetallic deposit has been mined since the 1950s, with 0.17 Mt Pb (1%), 0.37 Mt Zn (2.3%) and 1 800 t Ag (110 g/t). It was hosted by biotite/muscovite granites. The biotite granite was intruded by muscovite muscovite granite. Jiang et al. (2011) reported a LA-ICP-MS zircon U-Pb age of 240.5±1.2 Ma for the biotite granite and 234.3±3.2 Ma for the muscovite granite. In generally, from the western to eastern ore-block, the mineralization depth becomes shallower and Fe content of sphalerite decreases gradually. Seventy percent of Ag were found in the eastern ore-block (Zhu et al., 2006).

2.1 Structures

Over 40 EW- or NNW-striking faults were delineated to form a grid pattern and cross cut the muscovite/biotite granites (Zhu et al., 2006). The EW-striking faults are the main ore controlling structure. Two large diorite dikes in the western Meng'entaolegai (50–80 m long and 2–3 m wide) are controlled by the EW-striking faults and intruded the biotite/muscovite granites (Zhang et al., 2006; Zhu et al., 2006). The NNW-striking faults, extending <500 m along strike, are the main post-ore structures and are commonly orebody destructive. Many lamprophyre dikes intruded along the NNW-striking faults.

2.2 Orebody Characteristics

Over 40 orebodies were delineated, with the nine major ones shown in Fig. 2b. Individual orebody is generally 1 to 4 m (up to 8 m) thick and 400 to 2 000 m long (Zhang et al., 2006; Zhu et al., 2006). The mineralization styles in the western (Zn), middle (Zn-Pb) and eastern (Pb-Ag) ore-block are represented, respectively, by orebodies V8, V1 and V11. At Meng'entaolegai, ore textures include mainly vein and miarolitic, alteration styles include silicic, sericite, chlorite and carbonate.

Orebodies in the western ore-block are mainly Zn mineralization and the elevation is more than 70 m. The distance between main orebodies and branch orebodies is 50–200 m. Orebody V8 is the most representative in the western ore-block and 1.5–3 m thick and about 720 m long, and extends towards downward for ~400 m, strikes at 90º–95º, dips at 60º–70º to the SSW. As the most significant zinc orebody which contained 3%–5% Zn, orebody V8 is dominated by mineralized quartz vein or stringer that predominantly composed of sphalerite and quartz, with minor minerals including chalcopyrite, pyrite, stannite and galena. The comb-like and cavernous structures of quartz and sphalerite occasionally occur in some veins.

Table 1 Basic characteristics of the Ag-Pb-Zn deposits in the south segment of Great Xing'an Range metallogenic province

Deeposit	Reserves (10^4 t)	Grade	Host rocks and ages (Ma)	Mineralization ages (Ma)	Reference
Meng'entaolegai	Ag: 0.18 Pb: 37 Zn: 16	Ag: 110 g/t Pb: 1% Zn: 2.3%	Biotite granite (zircon U-Pb, 240.5±1.2) Muscovite granite (zircon U-Pb, 234.3±3.2)	Sericite Ar-Ar (182.3±3.8)	Zhang et al. (2006) Zhu et al. (2006) Jiang et al. (2011)
	Ag: 0.06 Pb+Zn: 18	Ag: 157 g/t Pb: 1.98% Zn: 1.96%	Permian slate	Sericite Ar-Ar (138.7±1)	Ruan et al. (2015) Zhai et al. (2018b, c, 2017)
Shuangjianzishan	Ag: 2.6 Pb: 110 Zn: 330	Ag: 400 g/t Pb: 2.8% Zn: 4.5%	Permian pelite Porphyritic monzogranite (zircon U-Pb, 253±3, 252±2.5)	Sphalerite Rb-Sr (132.7±3.9) Pyrite Re-Os (165±7.1)	Liu C H et al. (2016)
Bairendaba-Weiliesituo	Ag: 0.62 Zn: 200 Pb: 60 Cu: 15		Xilinhot metamorphic complex Quartz diorite (zircon U-Pb, 327±2)	Sericite Ar-Ar (133±1, 135±3)	Ouyang et al.（2014） Liu Y F et al. (2016)

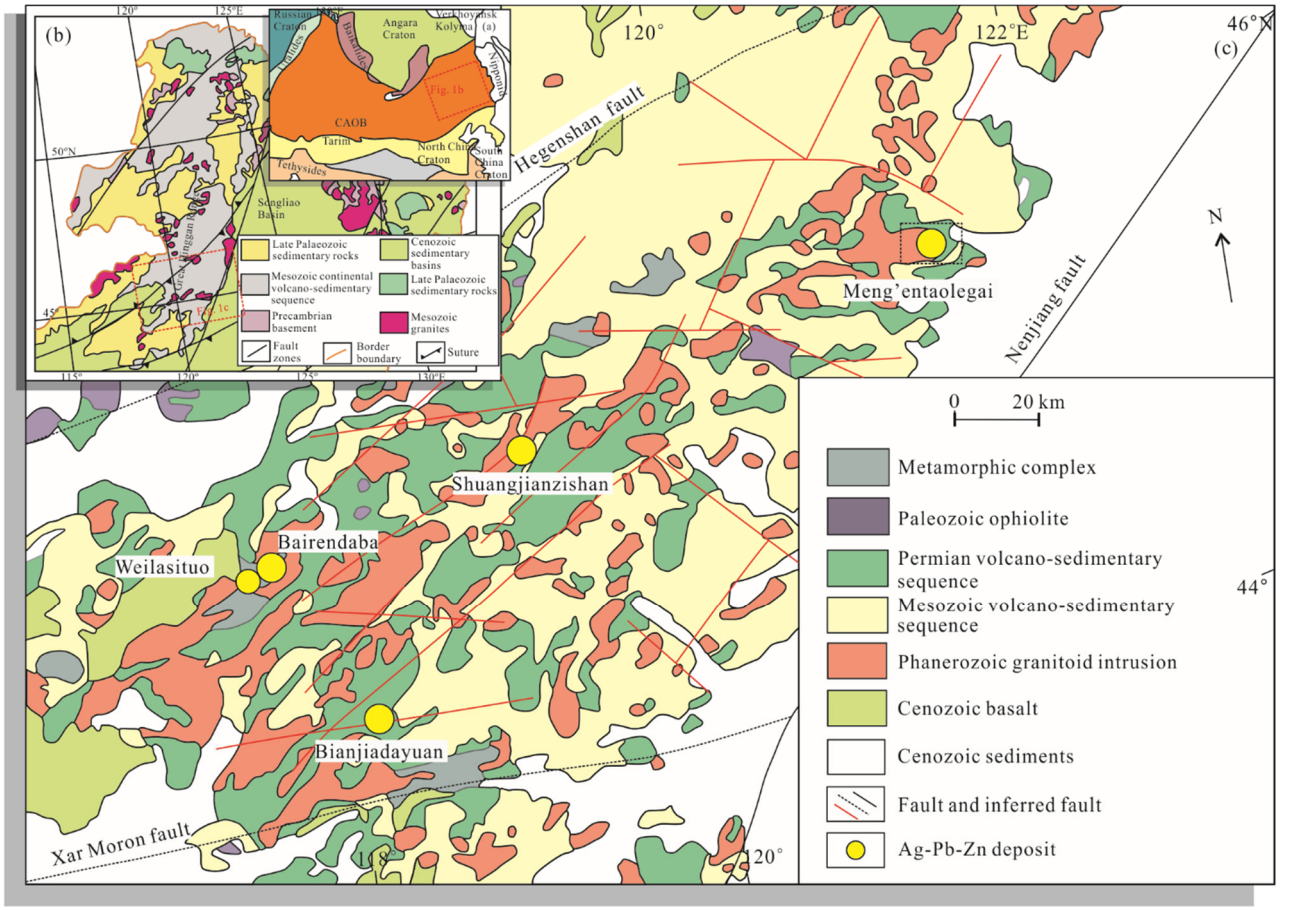

Figure 1. (a) Tectonic diagram for the Central Asian orogenic belt (modified from Waild and Zhou, 2015); (b) geologic map showing Mesozoic granites and tectonic divisions in the Great Hinggan Range (modified from Qi et al., 2005); (c) regional geologic map of the southern Great Hinggan Range (modified from Ouyang et al., 2014), showing the locations of the Meng'entaolegai and other Ag-Pb-Zn deposits.

Orebodies in the middle ore-block are mainly Zn-Pb mineralization and the elevation is more than 120 m. The distance between main orebodies and branch orebodies is relatively little about ~80 m. Orebody V1 is the largest in the middle orebody group and 1.5–3 m thick and more than 1 000 m long, strikes at 80º–90º, dips at 65º–75º to the SSW. It is dominated by mineralized quartz veins or net veins that predominantly composed of sphalerite, galena and quartz, with minor minerals including chalcopyrite, pyrite, stannite and acanthite. Specifically, galena and acanthite are not visible in some branch veins. The comb-like and cavernous structures of quartz occasionally occur in some veins.

Orebodies in the eastern ore-block are Ag-Pb mineralization and the elevation is more than 200 m. The different orebodies are very tight in spatial distribution in response to eastwardly convergent ore controlling structures. The distance between main orebodies and branch orebodies is ~70 m. Orebody V11 is the main orebody in the east orebody group and 1–4 m thick and more than 1 000 m long, and strikes at 70º–85º, dips at 70º–85º to the SE. It is dominated by mineralized quartz veins or veinlets that predominantly composed of galena, acanthite, native silver, pyrargyrite, sphalerite, and quartz, with minor minerals including chalcopyrite, pyrite, stannite, a little of calcite and other silver-bearing minerals.

There are an earlier mineralized quartz veins contained pyrite and minor arsenopyrite were cut off by Zn-Pb-Ag mineralized quartz veins in orebodies V8, V1 and V11. And the latest carbonate veins predominantly composed of smithsonite or calcite cut off the two kinds of earlier mineralized veins.

2.3 Mineralogy and Paragenesis

Metallic minerals in the veins of the Meng'entaolegai deposit are pyrite, sphalerite, galena, native silver and acanthite (Fig. 3), and the minor amounts of chalcopyrite, arsenopyrite, cassiterite, stannite and some Ag-bearing minerals are found; non-metallic minerals are quartz, and the minor amounts of calcite, smithsonite, are found.

According to mineral paragenesis and vein crosscutting relationship, the alteration/mineralization at Meng'entaolegai is divided into three stages (Fig. 3): (1) pre-ore stage: quartz-pyrite-arsenopyrite; (2) syn-ore stage: quartz-sphalerite± galena-pyrite-chalcopyrite±native silver±acanthite±calcite± stannite±other Ag-bearing minerals; (3) post-ore stage: calcite-smithsonite (Fig. 4). Brief descriptions of the major minerals were given below.

Quartz: The pre-ore quartz is always milky and fine-grained, and usually occur with perfect crystalline fine pyrite. The syn-ore quartz is milky and fine-coarse-grained, and usually shows comb-like structure.

Sphalerite and galena: Sphalerite occur mostly alone in the western ore-block. Sphalerite occurs more commonly with galena in the middle- and eastern ore-blocks. The sphalerite in orebody V8 is usually medium-grained, black and high in Fe (8.02 wt.%–12.96 wt.%, average 8.69 wt.%). The sphalerite in orebody V1 is usually fine or medium grained, brownish-black and medium in Fe (6.22 wt.%–8.59 wt.%, average 5.44 wt.%). The sphalerite in orebody V11 is usually fine-grained, brownish and low in Fe (3.62 wt.%–5.43 wt.%, average 3.71%) (Zhang et al., 2006). The galena in orebody V1 is always fine-medium irregular grain. The galena in orebody V11 shows perfect cubic shape.

Pyrite: The pre-ore stage pyrite shows nearly perfect cubic or pentagonal dodecahedron shapes. The syn-ore stage pyrite is always hypautomorphic, and replaced by sphalerite, galena and chalcopyrite.

Chalcopyrite: Chalcopyrite is only present in the syn-ore stage. The emulsion-like or lineated chalcopyrite were exsolved from sphalerite. Chalcopyrite also occurs with galena in the eastern ore-block.

Silver minerals: There are no Ag-bearing minerals in the western ore-block. Sphalerite and galena in the orebody V1 contain Ag about 453 ppm and 3 294 ppm, respectively (Zhang et al., 2004). Minor fine acanthite occurs in the middle ore-block, but is also of little economic significance. Economic endowment of Ag is mainly represented by acanthite, native silver and pyrargyrite, and minor Ag-bearing minerals (e.g., electrum, proustite, dyscrasite, pyrostilpnite, stephanite, diaphorite and freibergite) in the eastern ore-block.

2.4 Alteration and Mineralization

Hydrothermal alteration is widespread at Meng'entaolegai, with the most intense alteration occurring in and around mineralized Ag-Pb-Zn veins. Silicification is the most widespread expression of alteration type in the deposit, as fine silica within wall rock. Silicification are related with the pre-ore to post-ore stage mineralization. Chlorite which replaced plagioclase and biotite is mainly related to the pre-ore and syn-ore stage mineralization in the western ore-block. Sericite were ubiquitous in the syn-ore stage in all the three ore-blocks, plagioclase is completely or partially altered to sericite. Carbonatization is mainly related to the Ag mineralization and the post-ore alteration, which overprinted all previous alteration types. The type of alteration is generally related to different stage mineralization, while alteration zoning is undetected.

3 SAMPLES AND ANALYTICAL METHODS

3.1 Fluid Inclusions (FIs)

The samples for fluid inclusions microanalyses in this study are from pit galery or stope in the Meng'entaolegai deposit, and include (1) the quartz veins from orebody V8 associated with Zn mineralization; (2) the quartz veins from orebody V1 associated with Pb-Zn mineralization; and (3) the quartz veins from orebody V11 associated with Ag-Pb-Zn mineralization. More than 25 doubly polished thin sections were prepared for optical examination, from which 7 representative samples were chosen for microthermometric measurements.

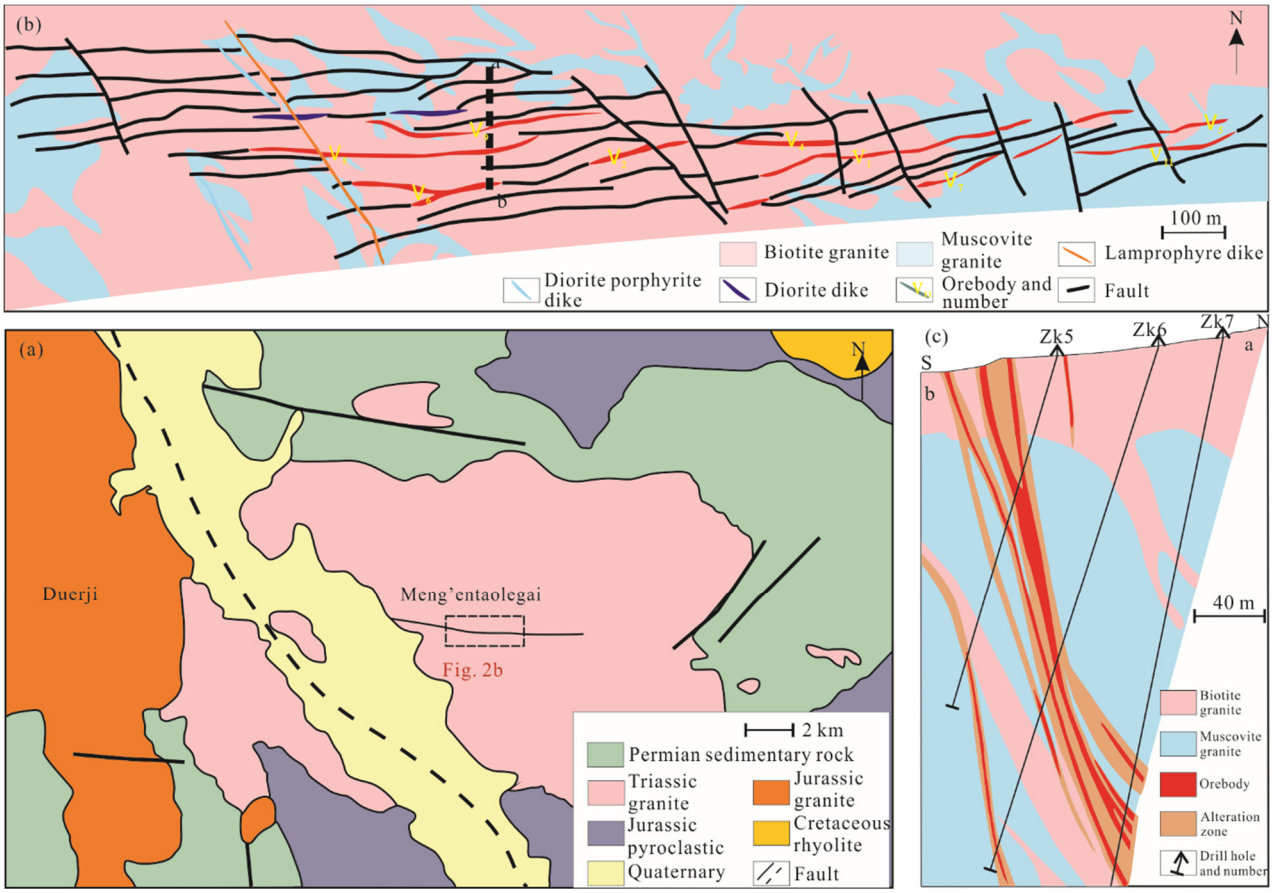

Figure 2. (a) Geologic map of the Meng'entaolegai deposit (dashed square region in Fig. 2b) (modified from Zhang et al., 2006); (b) dashed square region in Fig. 1b (modified from Zhang et al., 2006); (c) geologic cross-section of the Meng'entaolegai deposit (location showed in Fig. 2b) (modified from Zhang et al., 2006).

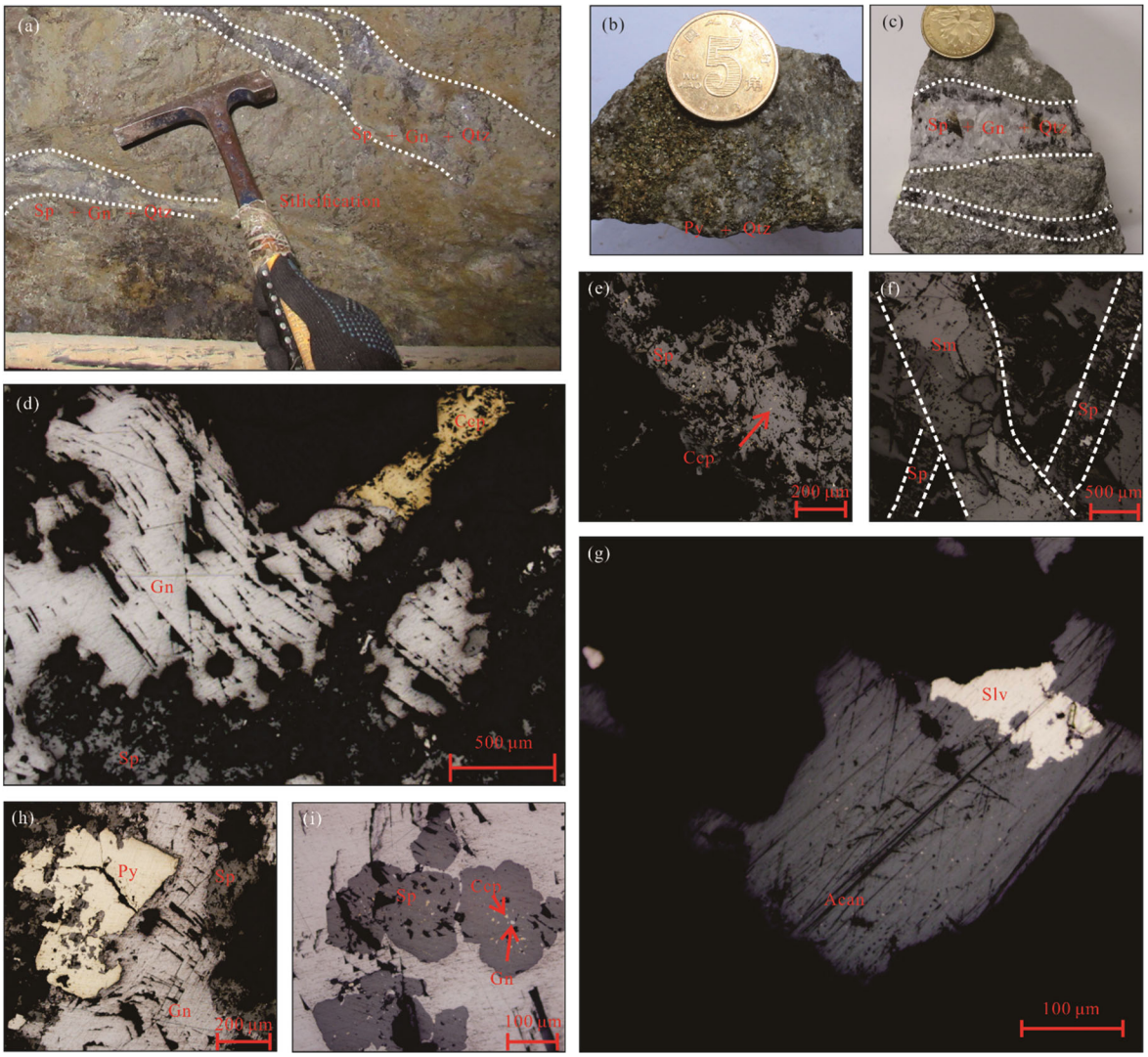

Figure 3. Photographs (a)–(c) and photomicrographs (d)–(i) of Ag-Pb-Zn ore veins and minerals. (a) Pb-Zn-Qtz vein accompanied by silification; (b) the pre-ore stage pyrite-quartz vein; (c) the syn-ore sphalerite-galena-quartz vein; (d) galena coexists with chalcopyrite and replaced by sphalerite; (e) and (i) emulsion-like chalcopyrite exsolved from sphalerite; (f) smithsonite vein cut sphalerite vein; (g) acanthite coexists with native silver; (h) pyrite replaced by galena and sphalerite. Abbreviations: Py. pyrite; Ccp. chalcopyrite; Sp. sphalerite; Gn. galena; Acan. acanthite; Slv. native silver; Sm. smithsonite; Qtz. quartz.

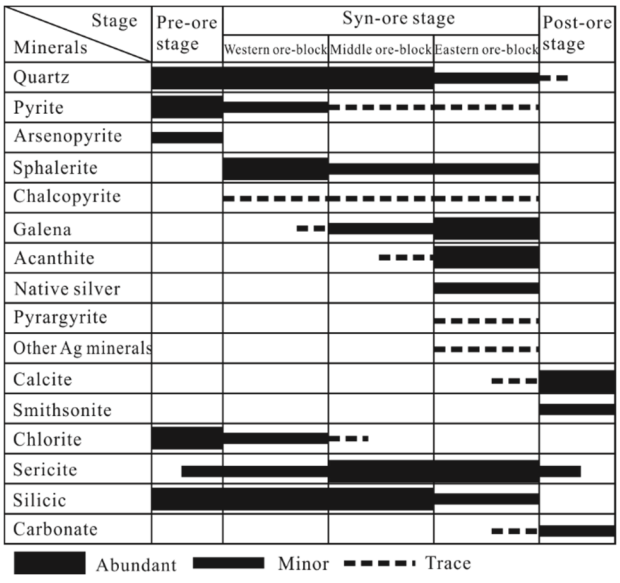

Figure 4. Paragenetic sequence of vein minerals in Meng'entaolegai deposit.

The Mn-9 and Mn-15 selected for microthermometric measurement were located in the middle and east of orebody V8, with elevations of approximately 180 and 230 m, respectively. The Mn-16 and Mn-18 samples were located in the middle of orebody V1, at an elevation of about 200 and 220 m. The samples of Mn-21, Mn-22 and Mn-26 were located in the west and middle part of the orebody V11, with elevations of about 200, 220 and 250 m, respectively.

Cooling and heating experiments for the FIs were conducted using a Linkam THMS 600 freezing-heating stage at the Key Laboratory of Geological Fluid, Jilin University, China. The estimated accuracy of temperatures is ±0.2 °C for temperatures from -180 to 31 °C, ±2.0 °C for temperatures above 31 °C. Heating/cooling rates were <10 °C/min, and were reduced to 1 to 0.1 °C/min near phase transformations. Freezing measurements were always conducted before heating measurements. To characterize dissolved salts, eutectic temperatures (Te) were measured following sequential freezing-heating procedures (Wang et al., 2017).

3.2 Isotope Analyses

Four syn-ore stage quartz samples for O-H isotope analyses were collected from orebodies V8 (1 sample) and V1 (1 sample) and V11 (2 samples).

Oxygen and hydrogen isotope compositions were determined using a MAT253-EM mass spectrometer at the Analytical Laboratory in Beijing Research Institute of Uranium Geology, China National Nuclear Corporation (CNNC). Prior to the analyses, the samples were carefully handpicked under a binocular microscope before extracting the oxygen and water. Oxygen was released from 10–20 mg of quartz grains using the BrF5 extraction technique in externally heated nickel reaction vessels (Clayton and Mayeda, 1963). The oxygen and hydrogen isotope analyses adopted the Standard Mean Ocean Water (SMOW) as a reference. The precision, determined by repeated analyses, is ±0.2‰ for both $\delta^{18}O$ and δD.

Four syn-ore sphalerite and galena samples for S-Pb isotope analyses were collected from orebodies V8 (1 sample) and V1 (1 sample) and V_{11} (2 samples).

Sulfide grains were carefully handpicked under a binocular microscope after the samples had been crushed, cleaned, and sieved to 40 to 60 mesh, to ensure >99% purity. Sulfur isotopes were analyzed using a Delta V Plus mass spectrometer at the same laboratory as the oxygen-hydrogen isotope analyses (Robinson and Kasakabe, 1975). The sulfur isotope values are reported using δ notation in per mil (‰) relative to V-CDT. Analytical precisions were within ±0.2‰.

Lead isotope measurements were conducted using a MAT-261 thermal ionization mass spectrometer (TIMS) at the same laboratory as the oxygen-hydrogen isotope analyses. Approximately 10–50 mg of powder for each sulfide sample were first leached in acetone to remove surface contamination and then washed by distilled water and dried at 60 °C in the oven. Each sulfide sample was dissolved in distilled $HF+HNO_3$ at 150 °C for seven days. The lead was separated on Teflon columns using an HBr-HCl wash and an elution procedure. The lead was loaded with a mixture of Sigel and H_3PO_4 onto a single Re filament and analyzed at 1 300 °C. The measured Pb isotope ratios were corrected for instrumental mass fractionation of 0.11% per atomic mass unit by references to repeated analyses of the NBS-981 Pb standard. The analytical precision of Pb isotope is better than ±0.09‰ (Wang et al., 2017).

4 RESULTS

4.1 Fluid Inclusion Petrography

FIs in syn-ore stage quartz from orebodies V8, V1 and V11 were analyzed using microthermometry. The criteria of Roedder (1984) and Hollister and Burruss (1976) were used to distinguish the different generations of FIs in the hydrothermal quartz. Primary, pseudo-secondary, and secondary FIs were observed. Primary inclusions are isolated or distributed randomly in intragranular crystals. The pseudo-secondary inclusions occur as trails in healed fractures, which do not cut grain boundaries. The planes of secondary inclusions cross-cut the mineral grains. These secondary inclusions were not analyzed using microthermometry, as it is possible that they formed late relative to the mineralization.

Three major types of inclusion were revealed based on phase assemblages at room temperature (25 °C): daughter-mineral-bearing (LVH-type), vapor-rich aqueous (VL-type), and liquid-rich aqueous (LV-type) (Fig. 5).

LVH-type FIs consist of a brine liquid, and a vapour bubble and a daughter mineral with a cubic form, which is identified as halite. The inclusions typically exhibit a negative-crystal, elliptical or sub-rounded shape and are 5–18 μm in size. Vapor bubbles account for 10%–25% of the total volume of the inclusions. LVH-type FIs occur in both isolation and as clusters in the syn-ore stage quartz of orebodies V8 and V1, and commonly coexist with VL-type FIs, indicating boiling features. These FIs account for ~10% of the total FIs. LVH-type FIs were further classified into three subtypes, LVH_1 FIs are homogenized by disappearance of halite; LVH_2 FIs are homogenized by simultaneous disappearance of vapor and halite; LVH_3 FIs are homogenized by disappearance of vapor.

VL-type FIs consist of vapor+liquid phases, with vapor phase accounting of >60 %. These FIs typically display are elliptical to sub-rounded in shape with a size range of 5 to 15 μm. They generally occur in clusters or are distributed randomly in the syn-ore stage quartz of orebodies V8 and V1, but are absent in orebody V11. These FIs account for ~20% of the total FIs and are homogenized to the vapour phase when heated.

LV-type FIs comprise a liquid phase and a vapour bubble at room temperature with vapor phase accounting of 15%–40%. These FIs are elliptical or irregular in shape, with a size range of 4–18 μm. They are commonly distributed in groups or isolated in veins of orebodies V8, V1 and V11. These FIs account for ~70% of the total FIs and are homogenized to the liquid phase when heated.

4.2 Fluid Inclusion Microthermometry

The results of microthermometry analyses of >280 FIs are presented in Table 2. The microthermometric data for FIs were calculated using the program of Steele MacInnis et al. (2012). Primary FIs of >5 μm in size, with a regular crystal shape and without evidence of necking, were chosen for microthermometry. Only a few VL-type FIs could be analyzed, owing to their low vapor-to-liquid ratio.

Orebody V8: LVH-(LVH_1 and LVH_2), VL- and LV-type FIs were identified in the syn-ore ore-bearing quartz. During freezing heating, the final ice-melting temperatures (Tm-ice) of the LV-type FIs ranged from -5 to -1.5 °C with calculated salinities of 2.6 wt.% to 7.9 wt.%. Final homogenization into the liquid phase was achieved at temperatures (Th-total) between 244 and 315 °C. The final ice-melting temperatures of the VL-type FIs range between -3.3 and -0.7 °C, corresponding to salinities of 1.2 wt.%–5.4 wt.% NaCl equivalent. Total homogenization of VL-type FIs to a vapor phase occurred at temperatures of 254–308 °C. The LVH_1-type FIs were homogenized to a single liquid phase by disappearance of halite at 263–294 °C and yielded salinities of 35.5 wt.%–37.7 wt.% NaCl. The LVH_2-type FIs were homogenized to a single liquid phase by simultaneous disappearance of vapor and halite at 270–281 °C and yielded salinities of 36 wt.%–36.8 wt.% NaCl.

Orebody V1: LVH-(LVH_1, LVH_2 and LVH_3), VL- and LV-type FIs were identified in the syn-ore ore-bearing quartz. During freezing heating, the final ice-melting temperatures (Tm-ice) of the LV-type FIs ranged from -7.1 to -2.2 °C with calculated salinities of 3.7 wt.% to 10.6 wt.%. Final homogenization into

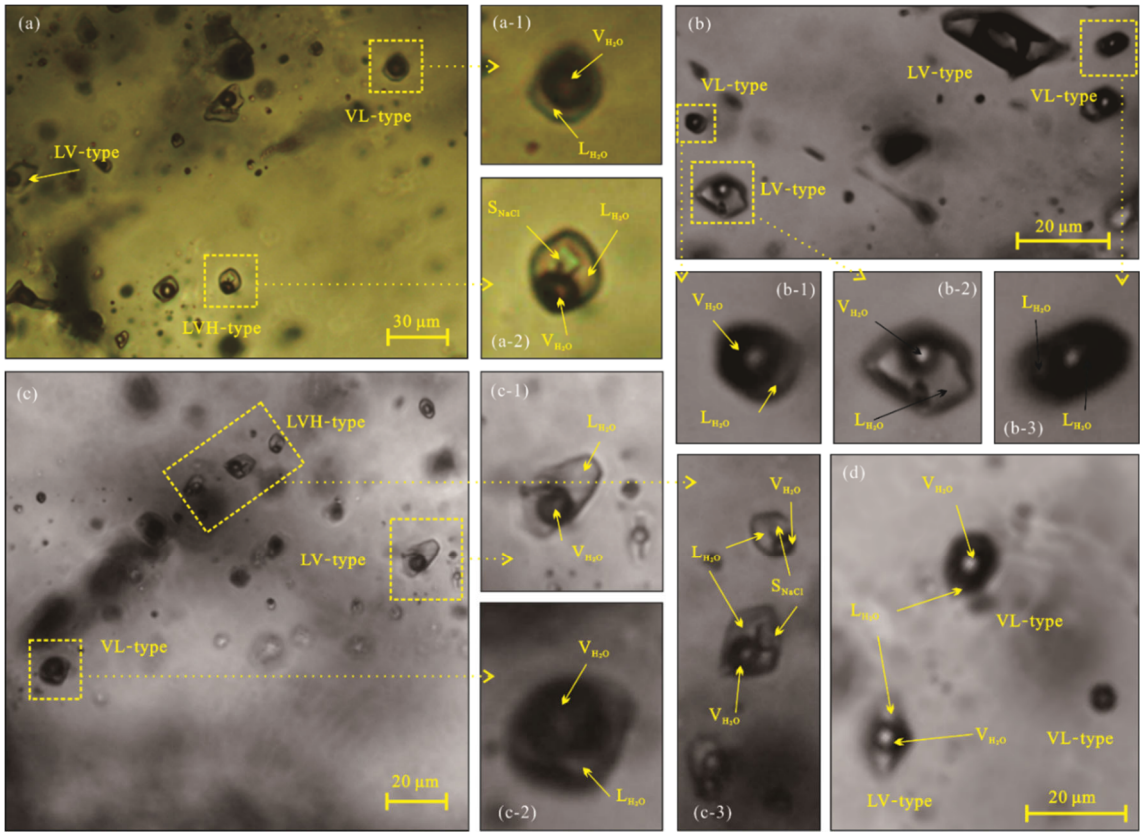

Figure 5. Photomicrographs of representative primary fluid inclusions in quartz from the Meng'entaolegai deposit. (a) Co-occurring LV-, VL- and LVH-type FIs within the same quartz crystal from orebody V8; a-1. VL-type FI; a-2. LVH-type FI; (b) co-occurring LV- and VL-type FIs within the same quartz crystal from orebody V8; b-1, VL-type FI; b-2, LV-type FI; B-3, VL-type FI; (c) co-occurring LV-, VL- and LVH-type FIs within the same quartz crystal from orebody V1; c-1. LV-type FI; c-2. VL-type FI; c-3. LVH-type FIs; (d) co-occurring LV- and VL-type FIs within the same quartz crystal from orebody V1.

the liquid phase was achieved at temperatures (Th-total) between 231 and 278 °C. Tm-ice of the VL-type FIs ranged from -2.6 to -0.5 °C with calculated salinities of 0.9 wt.%–4.3 wt.%. Final homogenization into the vapor phase was achieved at temperatures between 253 and 298 °C. The LVH_1-type FIs were homogenized to a single liquid phase by disappearance of halite at 254–265 °C and yielded salinities of 34.8 wt.%–35.5 wt.% NaCl. The LVH_2-type FIs were homogenized to a single liquid phase by simultaneous disappearance of vapor and halite at 261–268 °C and yielded salinities of 35.4 wt.%–35.9 wt.% NaCl. The LVH_3-type FIs were homogenized to a single liquid phase by disappearance of vapor at 264–281 °C. The NaCl daughter minerals within the inclusions dissolved at temperatures of 248–270 °C and yielded salinities of 34.5 wt.%–36 wt.% NaCl.

Orebody V11: Only one set of LV-type FIs was developed in the syn-ore ore-bearing quartz of this orebody. During freezing heating, Tm-ice of the VL-type FIs ranged from -5.8 to -1.5 °C with calculated salinities of 2.6 wt.%–8.5 wt.%. Final homogenization into the liquid phase was achieved at temperatures between 187 and 252 °C.

4.3 Hydrogen and Oxygen Isotopes

Hydrogen and oxygen isotope compositions were obtained from vein quartz that formed during syn-ore stage in orebodies V8, V1 and V11 are provided in Table 3 and Fig. 6. The calculated $\delta^{18}O_{H_2O}$ values for the ore fluid in equilibrium with quartz from three orebodies, utilizing the equations of quartz-water from Clayton et al., 1972; $\delta^{18}O_{quartz\text{-}SMOW}-\delta^{18}O_{H_2O}=3.38\times10^6/T^2-2.9$). The δD_{H_2O} and $\delta^{18}O_{H_2O}$ values are -131.1 and 6.8, respectively, in orebody V8. The δD_{H_2O} and $\delta^{18}O_{quartz}$ values are -130.9 and 5.7, respectively, in orebody V1. The δD_{H_2O} and $\delta^{18}O_{quartz}$ values are -123 to -123.5 and 0.8 to 1.4, respectively, in orebody V11. The H-O isotope data from FIs in sphalerite by Zhu et al. (2006) are also presented in Table 3 for comparison.

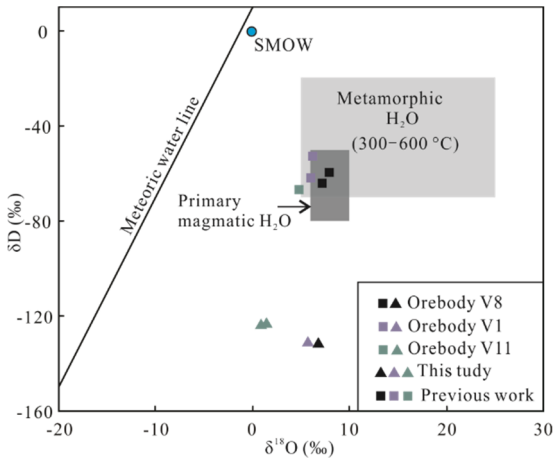

Figure 6. δD vs. $\delta^{18}O_{fluid}$ diagram of the syn-ore stage in three ore-blocks (modified from Taylor, 1974).

Table 2 Summary of microthermometric data on fluid inclusions of the Meng'entaolegai deposit

Sample No.	Type	T_e (°C)	$T_{m\text{-}ice}$ range (°C)	Avg. (%)	$T_{m\text{-}halite}$ range (°C)	Avg. (%)	$T_{h\text{-}L\text{-}V}$ range (°C)	Avg. (%)	T_h range (°C)	Avg. (%)	Salinity range (%)	Avg. (%)
Mn-9	LV	-21.5 to 23 (2)	-1.5 to -5 (29)	-3.3					253 to 311 (29)	277	2.6 to 7.9 (29)	5.4
Mn-9	VL	N. D.	-1.1 to -3 (11)	-1.8					271 to 308 (11)	285	1.9 to 5.0 (11)	3.1
Mn-9	LVH1	N. D.			271 to 294 (8)	279	267 to 286 (8)	275	271 to 294 (8)	279	36.1 to 37.7 (9)	36.6
Mn-9	LVH2	N. D.			279 (1)	279	279 (1)	279	279 (1)	279	36.6 (1)	36.6
Mn-15	LV	-20.3 to 22.4 (3)	-2.3 to -5 (33)	-3.6					244 to 295 (33)	270	3.9 to 7.9 (33)	5.8
Mn-15	VL	N. D.	-0.7 to -3.3 (8)	-1.8					254 to 295 (8)	277	1.2 to 5.4 (8)	3.1
Mn-15	LVH1	N. D.			263 to 280 (8)	273	246 to 276 (8)	267	263 to 280 (8)	273	35.5 to 36.7 (8)	36.1
Mn-15	LVH2	N. D.			270 to 281 (4)	277	270 to 281 (4)	277	270 to 281 (4)	277	36 to 36.8 (4)	36.5
Mn-16	LV	N. D.	-2.6 to -7.1 (20)	-4.4					236 to 278 (20)	259	4.3 to 10.6 (20)	7
Mn-16	VL	N. D.	-0.5 to -2.6 (9)	-1.6					261 to 298 (9)	272	0.9 to 4.3 (9)	2.8
Mn-16	LVH1	N. D.			254 to 265 (4)	260	250 to 263 (4)	258	254 to 265 (4)	260	34.8 to 35.5 (4)	35.2
Mn-16	LVH3	N. D.			259 to 270 (3)	264	269 to 281 (3)	273	269 to 281 (3)	273	35.3 to 36 (3)	35.6
Mn-18	LV	-23 (1)	-2.2 to -6 (31)	-4.5					231 to 278 (31)	251	3.7 to 9.2 (31)	7.1
Mn-18	VL	N. D.	-0.6 to -1.9 (11)	-1.4					253 to 281 (11)	267	1.1 to 3.2 (7)	2.4
Mn-18	LVH1	N. D.			256 to 265 (8)	260	248 to 263 (8)	256	256 to 265 (8)	260	34.9 to 35.5 (9)	35.2
Mn-18	LVH2	N. D.			261 to 268 (4)	265	261 to 268 (4)	265	261 to 268 (4)	265	35.4 to 35.9 (4)	35.6
Mn-18	LVH3	N. D.			248 to 254 (3)	250	264 to 273 (3)	268	264 to 273 (3)	268	34.5 to 34.9 (3)	34.7
Mn-21	LV	N. D.	-2.8 to -5.8 (37)	-4.3					212 to 252 (37)	232	4.6 to 8.9 (37)	6.9
Mn-22	LV	N. D.	-1.5 to -4.8 (27)	-3.7					187 to 223 (27)	206	2.6 to 7.6 (27)	6
Mn-26	LV	-20.1 to -21.2 (2)	-3.1 to -5.2 (29)	-3.9					198 to 245 (29)	222	5.1 to 8.1 (29)	6.4

Number of inclusins measured is given in parentheses; N. D. not determined; T_e. eutectic temperature; $T_{m\text{-}ice}$. ice-melting temperature; $T_{m\text{-}halite}$. ice-melting temperature for halite; $T_{h\text{-}L\text{-}V}$. homogenization temperature of vapor and liquid for LVH-type inclusion; T_h. homogenization temperature; the location of the samples is described in detail in the paper.

Table 3 Summary of hydrogen and oxygen isotope compositions of the Meng'entaolegai deposit

Sample No.	Sample location	Mineral	$\delta^{18}D_{V\text{-}SMOW}$ (‰)	$\delta^{18}O_{quartz\text{-}SMOW}$ (‰)	T (°C)	$\delta^{18}O_{H_2O\text{-}SMOW}$ (‰)	Data source
M-6	Orebody V8	Sphalerite	-64.2			7.2	Zhu et al. (2006)
M-15	Orebody V8	Sphalerite	-52.8			6.1	Zhu et al. (2006)
M-23	Orebody V1	Sphalerite	-59.6			7.9	Zhu et al. (2006)
M-25	Orebody V1	Sphalerite	-61.7			5.8	Zhu et al. (2006)
M-33	Orebody V11	Sphalerite	-66.9			4.8	Zhu et al. (2006)
Mn-15	Orebody V8	Quartz	-131.1	15.4	270	6.8	This study
Mn-18	Orebody V1	Quartz	-130.9	15.2	250	5.7	This study
Mn-21	Orebody V11	Quartz	-123	11.9	230	1.4	This study
Mn-24	Orebody V11	Quartz	-123.5	11.3	230	0.8	This study

Table 4 Summary of sulfur isotope compositions of the Meng'entaolegai deposit

Sample No.	Sample locality	Mineral	$\delta^{34}S$ (‰)	T (°C)	$\delta^{34}S_{H_2S}$ (‰)	Data source
Mn-1	Orebody V8	Sphalerite	2.1	270	2.4	This study
Mn-3	Orebody V1	Sphalerite	1.2	250	0.8	This study
Mn-5	Orebody V11	Sphalerite	4.1	230	3.7	This study
Mn-7	Orebody V11	Galena	-0.8	230	1.7	This study
M4	Orebody V8	Sphalerite	1.9	270	1.6	Zhu et al. (2006)
M5	Orebody V8	Sphalerite	-0.8	270	-1.1	Zhu et al. (2006)
M6	Orebody V8	Sphalerite	1.3	270	1	Zhu et al. (2006)
M2	Orebody V8	Galena	0.7	270	2.8	Zhu et al. (2006)
M8	Orebody V8	Galena	-1.6	270	0.5	Zhu et al. (2006)
M9	Orebody V8	Galena	-0.2	270	1.9	Zhu et al. (2006)
M12	Orebody V8	Galena	0.1	270	2.2	Zhu et al. (2006)
M29	Orebody V1	Sphalerite	0.3	250	-0.1	Zhu et al. (2006)
M25	Orebody V1	Sphalerite	2.4	250	2	Zhu et al. (2006)
M21	Orebody V1	Sphalerite	2.9	250	2.5	Zhu et al. (2006)
M30	Orebody V1	Galena	-0.1	250	2.2	Zhu et al. (2006)
M22	Orebody V1	Galena	0.2	250	2.5	Zhu et al. (2006)
M41	Orebody V11	Sphalerite	1.8	230	1.4	Zhu et al. (2006)
M32	Orebody V11	Sphalerite	2.3	230	1.9	Zhu et al. (2006)
M35	Orebody V11	Sphalerite	1.2	230	0.8	Zhu et al. (2006)
M42	Orebody V11	Galena	1.2	230	3.7	Zhu et al. (2006)
M39	Orebody V11	Galena	0.9	230	3.4	Zhu et al. (2006)
M33	Orebody V11	Galena	1.5	230	4	Zhu et al. (2006)

4.4 Sulfur Isotopes

Sulfide S isotope compositions were obtained for the three orebodies at Meng'entaolegai, and were compared with published data (Zhu et al., 2006) (Table 4). The sphalerite and galena $\delta^{34}S$ values of orebody V8 are of -0.8 to 2.1 and -1.6 to 0.7, respectively, whilst those of orebody V1 are of -0.1 to 2.5 and 2.2 to 2.5, respectively. The sphalerite and galena $\delta^{34}S$ values of orebody V11 are of 0.8 to 3.7 and 1.7 to 4, respectively. The mean isotopic composition of H_2S in the ore-forming fluid ($\delta^{34}S$ (H_2S)) are of -1.1 to 2.8, -0.1 to 2.5 and 0.8 to 4 in orebodies V8, V1 and V11, respectively, utilizing the equations from Ohtomo and Goldhaber, 1997; $\delta^{34}S(galena)–\delta^{34}S(H_2S)= -630\ 000/T^2$; $\delta^{34}S(sphalerite)–\delta^{34}S(H_2S)=100\ 000/T^2$ (T in kelvins)).

4.5 Lead Isotopes

Radiogenic lead isotopic compositions for the sphalerite and galena are presented in Table 5 and Fig. 7, obtained by this study and previous studies (Zhu et al., 2006). The sulfide $^{206}Pb/^{204}Pb$, $^{207}Pb/^{204}Pb$ and $^{208}Pb/^{204}Pb$ values are, respectively, orebody V8 (18.137–18.308, 15.421–15.564, 37.713–38.116), orebody V1 (18.179–18.271, 15.429–15.551, 37.718–38.131), and orebody V11 (18.131–18.283, 15.43–15.54, 37.69–38.152).

4.6 Activities Estimate

Activities are significant parameters for constructing thermodynamic models and restoring hydrothermal metallogenic environment. They can be estimated by (extended) Debye-Huckel equation based on the species concentrations. The average concentrations of total Zn and Pb in the syn-ore stage fluids were about 247 ppm and 65 ppm (orebody V8), 224.3 ppm and 59.67 ppm (orebody V1), and 217 ppm and 62 ppm (orebody V11), respectively (Zhang et al., 2006). The data were obtained by ICP-MS analysis for the fluids extracted from FIs by decrepitation at suitable temperatures, more details refer to Zhang et al. (2006) and Su et al. (2001). The salinity of the main ore stage fluid in the orebodies V8, V1 and V11 were about 5.6 wt.%, 7.1 wt.%, 6.4 wt.% NaCl eqv. (Table 2). If the ore-forming fluid is regarded as a simple NaCl-H_2O system, the estimated molality of total Cl in the fluids could be calculated using the above FI data. Thus, the concentrations and activity coefficients of the major aqueous species (Zn^{2+}, Pb^{2+} and chloride complex) were obtained using the EQBRM program, for simplified NaCl-Pb or Zn-H_2O system (Greg and David, 1993). The results approximately represent the actual species activities in the hydrothermal system (Table 6). Metal-organic species, minor ions and

molecules were not considered here due to the lacking of the biogenetic mineralization evidence, and the dispensability of Zn/Pb(OH) in acidic or neutral environment (Hennet et al., 1988). Debye-Huckel A parameter (in Debye-Huckel equation) came from Helgeson and Kirkham (1974), and the slight effect of pressure to A parameter was ignored.

Table 5 Summary of lead isotope compositions of the Meng'entaolegai deposit

Sample No.	Sample locality	Mineral	$^{206}Pb/^{204}Pb$	$^{207}Pb/^{204}Pb$	$^{208}Pb/^{204}Pb$	Data source
Mn-1	Orebody V8	Sphalerite	18.271	15.536	38.084	This study
Mn-3	Orebody V1	Sphalerite	18.271	15.551	38.131	This study
Mn-5	Orebody V11	Sphalerite	18.248	15.475	38.152	This study
Mn-7	Orebody V11	Galena	18.166	15.530	37.842	This study
M-2	Orebody V8	Galena	18.137	15.421	37.713	Zhu et al. (2006)
M-3	Orebody V8	Galena	18.203	15.448	37.878	Zhu et al. (2006)
M-12	Orebody V8	Galena	18.308	15.564	38.116	Zhu et al. (2006)
M-14	Orebody V8	Galena	18.216	15.461	37.845	Zhu et al. (2006)
M-19	Orebody V1	Galena	18.191	15.467	38.109	Zhu et al. (2006)
M-21	Orebody V1	Galena	18.251	15.44	37.718	Zhu et al. (2006)
M-24	Orebody V1	Galena	18.224	15.429	37.731	Zhu et al. (2006)
M-28	Orebody V1	Galena	18.179	15.452	37.824	Zhu et al. (2006)
M-33	Orebody V11	Galena	18.242	15.522	37.925	Zhu et al. (2006)
M-34	Orebody V11	Galena	18.131	15.437	37.690	Zhu et al. (2006)
M-36	Orebody V11	Galena	18.155	15.430	37.710	Zhu et al. (2006)
M-41	Orebody V11	Galena	18.283	15.540	37.945	Zhu et al. (2006)
M-43	Orebody V11	Galena	18.239	15.498	37.892	Zhu et al. (2006)

Table 6 Summary of estimated species concentrations and activity coefficient of Stage 2 fluid in three orebodies

Sample locality	Species	Final concentrations	Activity coefficient	GAMMA iteration No.
Orebody V8	Zn^{2+}	1.01×10^{-7}	4.42×10^{-2}	4
	$ZnCl^{+}$	1.21×10^{-3}	4.59×10^{-1}	4
	$ZnCl_2$	6.80×10^{-4}	1	4
	$ZnCl_3^{-}$	4.28×10^{-5}	4.59×10^{-1}	4
	$ZnCl_4^{2-}$	1.17×10^{-3}	4.42×10^{-2}	4
	Pb^{2+}	9.73×10^{-8}	4.42×10^{-2}	4
	$PbCl^{+}$	7.48×10^{-6}	4.59×10^{-1}	4
	$PbCl_2$	6.88×10^{-5}	1	4
	$PbCl_3^{-}$	6.61×10^{-5}	4.59×10^{-1}	4
	$PbCl_4^{2-}$	1.15×10^{-4}	4.42×10^{-2}	4
Orebody V1	Zn^{2+}	1.39×10^{-7}	6.01×10^{-2}	5
	$ZnCl^{+}$	1.04×10^{-3}	4.95×10^{-1}	5
	$ZnCl_2$	5.90×10^{-4}	1	5
	$ZnCl_3^{-}$	4.69×10^{-5}	4.95×10^{-1}	5
	$ZnCl_4^{2-}$	1.28×10^{-3}	6.01×10^{-2}	5
	Pb^{2+}	9.26×10^{-8}	6.01×10^{-2}	5
	$PbCl^{+}$	6.78×10^{-6}	4.95×10^{-1}	5
	$PbCl_2$	6.31×10^{-5}	1	5
	$PbCl_3^{-}$	6.60×10^{-5}	4.95×10^{-1}	5
	$PbCl_4^{2-}$	1.12×10^{-4}	6.01×10^{-2}	5
Orebody V11	Zn^{2+}	3.863×10^{-7}	7.498×10^{-2}	5
	$ZnCl^{+}$	1.357×10^{-3}	5.233×10^{-1}	5
	$ZnCl_2$	6.279×10^{-4}	1	5
	$ZnCl_3^{-}$	5.044×10^{-5}	5.233×10^{-1}	5
	$ZnCl_4^{2-}$	1.130×10^{-3}	7.498×10^{-2}	5
	Pb^{2+}	2.241×10^{-7}	7.498×10^{-2}	5
	$PbCl^{+}$	1.217×10^{-5}	5.233×10^{-1}	5
	$PbCl_2$	9.085×10^{-5}	1	5
	$PbCl_3^{-}$	8.319×10^{-5}	5.233×10^{-1}	5
	$PbCl_4^{2-}$	1.128×10^{-4}	7.498×10^{-2}	5

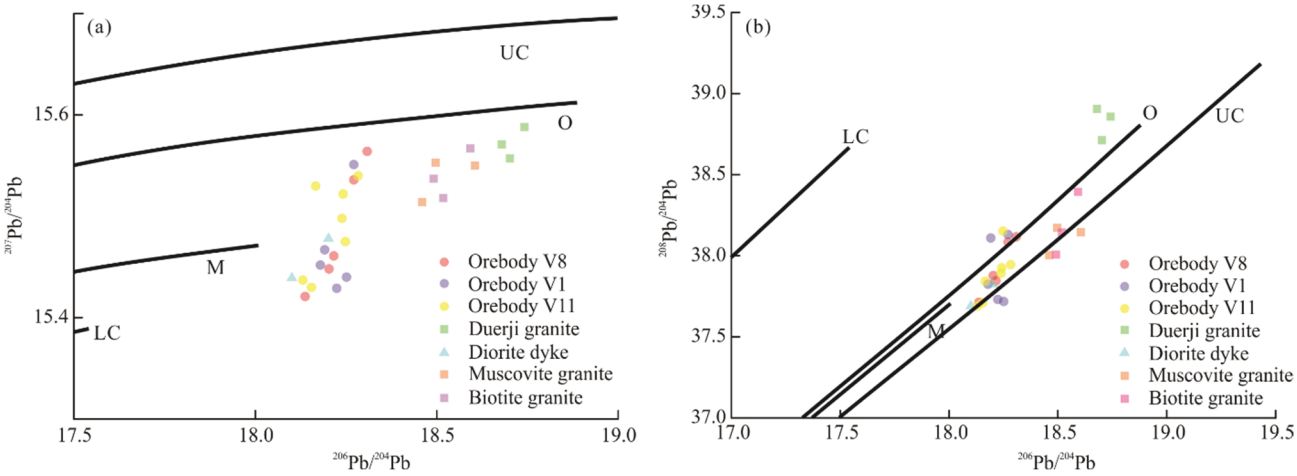

Figure 7. Lead isotopic compositions of sulfides and wall-rocks in the Jidetun deposit. (a) $^{207}Pb/^{204}Pb$ vs. $^{206}Pb/^{204}Pb$; (b) $^{208}Pb/^{204}Pb$ vs. $^{206}Pb/^{204}Pb$. Abbreviations: UC. Upper crust; O. orogen; M. mantle; LC. lower crust. Average growth lines are from Zartman and Doe (1981).

5 DISCUSSION

5.1 Fluid Boiling and Pressure Estimate

The Meng'entaolegai deposit shows evidence of fluid boiling in orebodies V8 and V1. Firstly, the abundance of V-type FIs indicates significant volumes of the vapor phase during fluid trapping (Fig. 5). Secondly, co-occurring LV-, VL- and LVH-type FIs were found (Fig. 5) (Chi et al., 2016). VL- and LVH-type FIs are homogenized at similar temperatures, indicating that they were trapped simultaneously. LV-type FIs have relatively higher T_h and represent fluid trapped in single phase (Klemm et al., 2007) (Fig. 8). Thirdly, LVH-type FIs are homogenized by different modes.

Trapping pressure can be estimated only when the actual trapping temperature is known or if the FIs were trapped under immiscible or boiling conditions, and by using using the program of Steele-MacInnis et al. (2012). A lack of evidence of fluid boiling in V11 allows only the minimum trapping temperatures and pressures to be estimated (Zhu et al., 2015).

In this study, four groups of the coexisting VL- and LVH-type inclusions (which represent boiling) were used to estimate the trapping pressure (Fig. 9; Chi and Lu, 2008; Goldstein, 2001). The estimated trapping pressures for boiling-1 and -2 in V8 are 60–71 bar. The estimated trapping pressures for boiling-3 and -4 in V1 are 44–59 bar. The calculated pressures of LVH FIs with $T_{m\text{-halite}}>T_{h\text{-L-V}}$ were higher and largely exceeds other FI pressure. We propose that the abnormal pressure reflect accidental trapping of halite (Chi and Lu, 2008; Goldstein, 2001). For FIs in orebody V11, the homogenize to liquid at temperatures between 253.2 and 187 °C. The estimated minimum corresponding pressure is below 50 bars.

5.2 Fluid Properties and Evolution

The homogenization temperatures interval of FIs in three is around 200–300 °C, with a salinity range of 0.937 7 wt.%–37.7 wt.% NaCl eqv., indicating characteristics of a medium-temperature and medium-salinity fluid. Furthermore, no aqueous carbonic FIs were observed, and limited eutectic temperatures are near -21 °C and suggest sodium is the dominant cation in the fluid, which imply an H_2O-NaCl fluid system. Four major distribution trends of FI population, according to their homogenization temperatures (T_h) and salinity (or ice-melting temperature ($T_{m\text{-ice}}$)) were illustrated in Fig. 10 (Wilkinson, 2001; Hedenquist and Henley, 1985).

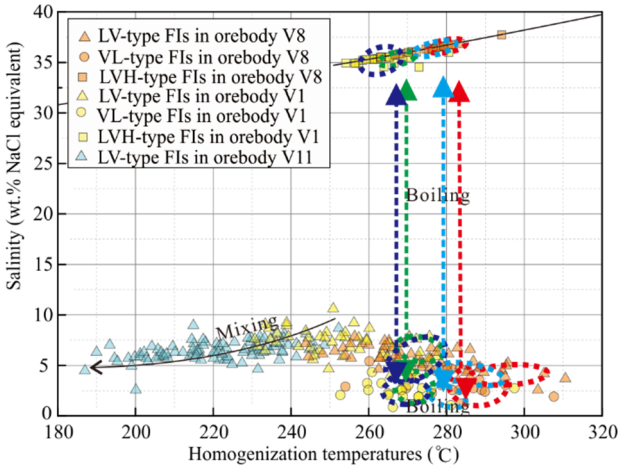

Figure 8. Summary plot of microthermometric measurements of FIs. Four groups of the coexisting LV- VL- and LVH-type inclusions (which represent boiling) were circled. VL- and LVH-type FIs are homogenized at similar temperatures, indicating that they were trapped simultaneously. LV-type FIs have relatively higher Th and represent fluid trapped in single phase.

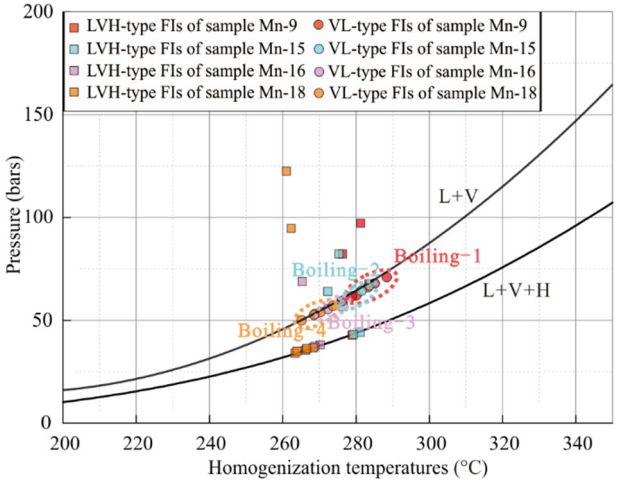

Figure 9. Temperature-pressure projection of the three-dimensional H_2O-NaCl phase diagram after Driesner and Heinrich (2007), modified from Klemm et al. (2007). Four groups of the coexisting VL- and LVH-type inclusions (which represent boiling) were plotted in this figure.

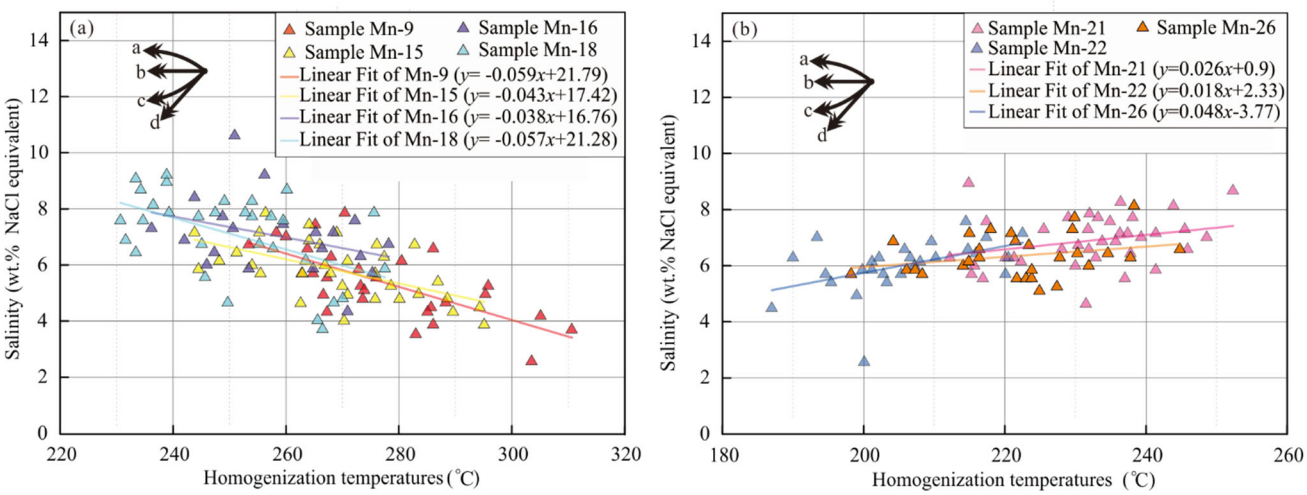

Figure 10. Summary plot of microthermometric measurements of LV-type FIs. (a) The linear fit results of FIs from orebodies V8 and V1 samples; (b) linear fit results of FIs from orebody V11 samples. Diagram showing four typical trends of distribution of fluid inclusion population, according to their homogenization temperature and salinity (or their ice-melting temperature, $T_{m\text{-}ice}$) (after Hedenquist and Henley (1985); Wilkinson (2001)). a. Boiling in a volatile-free system; b. cooling or pressurization; c. boiling with effervescence, in a volatile-rich system; d. dilution due to mixing with cold and low-salinity water.

The boiling (or effervescence in volatile-rich systems) and/or fluid mixing commonly provide the necessary conditions for effective ore precipitation in a limited rock volume (Wilkinson, 2011). The occurrence of VL- and LVH-type FIs (Fig. 5) in the syn-ore stage mineralized quartz veins of orebodies V8 and V1 provide fluid boiling evidence for effective ore deposition to the western and middle ore-blocks (Fan et al., 2011).

From Fig. 10a, it is indicated that the salinity increase with the T_h drop, are in response to continuous boiling of the syn-ore stage in V8 and V1 orebodies. Being the strong partitioning of salts into the liquid like phase (Wilkinson, 2011), the residual liquid becomes more saline in boiling process. In addition, as a result of adiabatic expansion, the liquid phase may also undergo cooling (Wilkinson, 2011). In contrast, from Fig. 10b, the salinity decrease with the T_h drop, implies fluid mixing process between high temperature-salinity fluid and low temperature-salinity fluid in orebody V11.

We propose the following fluid evolution process (Fig. 8): Continuous fluid boiling may caused the fluid salinity increase. The mixing process in the eastern ore-block may have caused the fluid to change into a low salinity fluid again during cooling. The boiling may be critical for the mineralization in the western and middle ore-blocks, whereas fluid mixing may be important for the mineralization in the eastern ore-block. We attribute the precipitation of galena and minor acanthite in orebody V1 to continuous boiling, which saturated the Zn, Pb and Ag in the the syn-ore stage ore-forming fluids.

The H-O isotopic compositions provide further evidence of fluid evolution from a magmatic hydrothermal system. The δD of FIs fluids in coexisting quartz are lower than that in sphalerite. We attribute the difference to secondary inclusions which has low δD. In a bivariate δD vs. $\delta^{18}O_{H_2O}$ plot (Fig. 6), samples from V8 and V1 orebodies plot in the primary magmatic water field, suggesting that initial ore-forming fluids were dominated by magmatic water. Samples from orebody V11 display lower $\delta^{18}O_{H_2O}$ values than those from orebodies V8 and V1. These values plot in the magmatic water field or between the magmatic water field and the meteoric water line, suggesting that ore-forming fluids had a mixed magmatic meteoric origin.

5.3 Physicochemical Conditions of Hydrothermal Fluids

Temperatures and pressures for the syn-ore stage in orebodies V8, V1 and V11 were estimated from FI data. In this section, we assess the relative important of change in pH, f_{O_2} and total S on mineralization at Meng'entaolegai deposit by evaluating the mineral stabilities using major aqueous species acticities and thermodynamic data for the ore minerals, water and aqueous species from the SUPCRT92 database (Johnson et al., 1992). The log f_{O_2}-pH diagrams have been constructed. The total sulfur concentration in ore-forming fluids was generally considered to be 0.1 to 0.001 mol/kg H_2O at various temperatures (Giggenbach, 1982; Ohmoto, 1972), although some FI analyses yielded lower concentrations (Maanijou et al., 2012). Here, total aqueous S concentrations were set to 0.01 or 0.001. The detailed discussion about physicochemical conditions of hydrothermal fluid in three ore-blocks is given in Appendix A.

The physicochemical conditions were shown by the red area in Fig. 11. The syn-ore fluids in the orebodies V8 and V1 were acidic, high f_{O_2}, sulfur-poor and $\delta S^{34}(\Sigma S)$=2.8(2.5). The similar conditions imply that the mineralization in the western and middle ore-blocks was caused by single fluid boiling. In contrast, the acidic fluids gradually neutralized, and are characterized by low f_{O_2}, sulfur-rich and with $\delta S^{34}(\Sigma S)$=0.5 in orebody V11. This divergent chemical condition cannot be reconciled by the action of a single fluid (Skirrow and Walshe, 2002), which is consistent with the previous FI microthermometry and H-O isotope. Therefore, we consider that higher pH caused by fluid mixing was the key of mineralization in the eastern ore-block and especially Ag-bearing minerals, e.g., native silver and acanthite. The elements of Zn, Pb and Ag always form Cl complexes and are transported by acidic hydrothermal solution (Robinson et al., 1973). There may be several orders of magnitude

difference for the necessary activity of metal ion when metal precipitated in acid and neutral solution (Fig. 11). For instance, for the syn-ore stage fluids in the middle ore-block, the acanthite did not precipitate until the activity of Ag^+ ion was over 10^{-9} m based on log f_{O_2}-pH phase diagram. In contrast, for the syn-ore stage fluids in the eastern ore-block, the acanthite still precipitated when the activity of Ag^+ ion was just 10^{-12} m. Under this mechanism, pH changes likely played a crucial role in precipitation of Ag-bearing minerals.

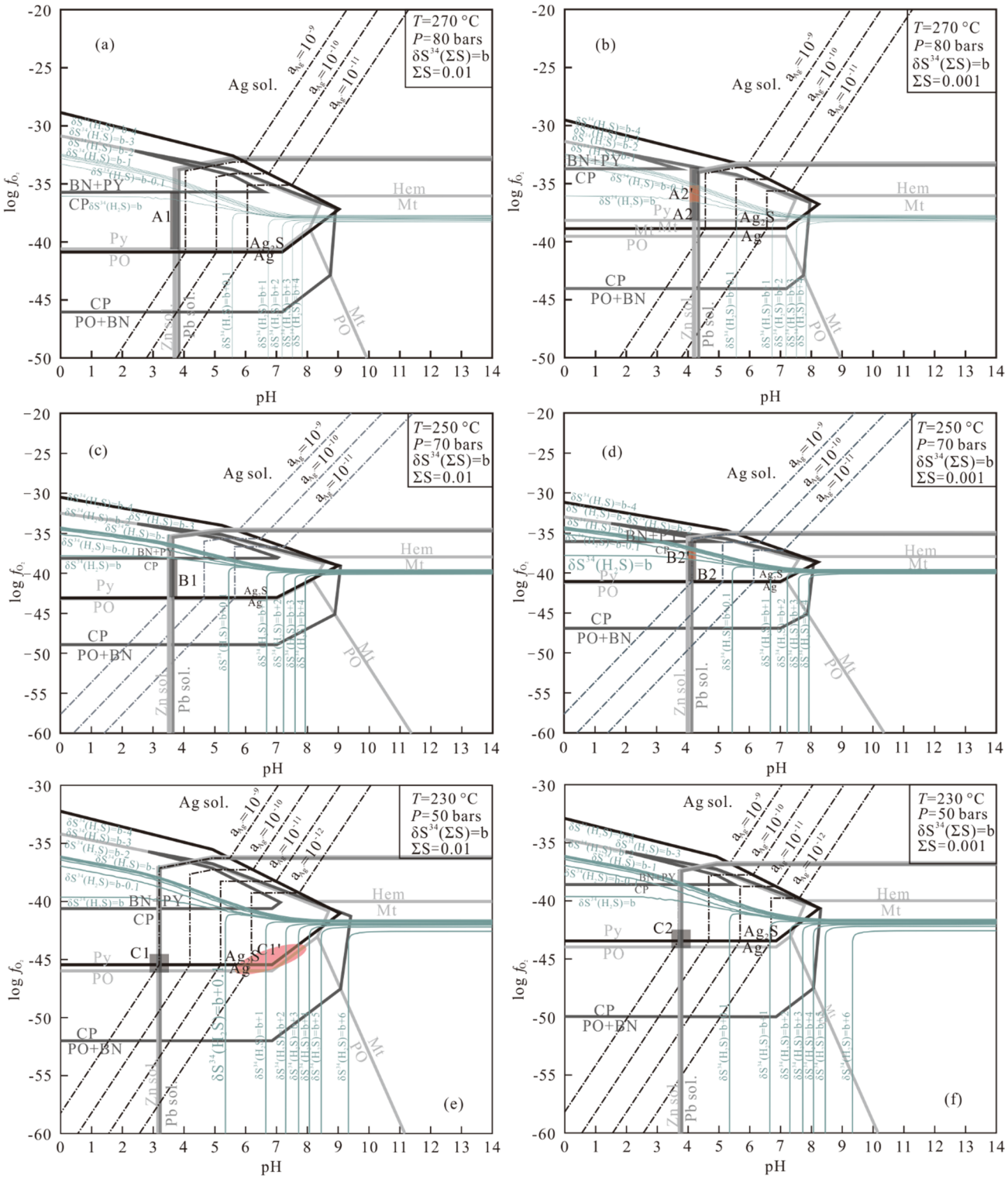

Figure 11. log f_{O_2}-pH diagram showing solubility and stability relationships of minerals during the syn-ore stage and illustrating the effects of f_{O_2}-pH changes on the sulfur isotopic compositions of minerals. (a) In orebody V8 at 270 °C, 80 bars and Total *S*=0.01; (b) in orebody V8 at 270 °C, 80 bars and Total *S*=0.001; (c) in orebody V1 at 250 °C, 70 bars and Total *S*=0.01; (d) in orebody V1 at 250 °C, 70 bars and Total *S*=0.001; (e) in orebody V11 at 250 °C, 50 bars and Total *S*=0.01; (f) in orebody V11 at 250 °C, 50 bars and Total *S*=0.001. Red area represents physicochemical conditions of hydrothermal fluids. Abbreviations: CP. chalcopyrite; PO. pyrrhotite; PY. pyrite; Mt. magnetite; Hem. hematite; BN. bornite.

5.4 Source of Materials

Sulfur isotopes are an important tool for determining the source of metals in ore deposits. The mean isotopic composition of sulfur in the ore-forming fluid ($\delta^{34}S(\Sigma S)$) has been estimated to be 2.8, 2.5, 0.5 in orebodies V8, V1, V11, respectively. These values are consistent with sulfur being derived from a magma source. The detailed discussion about $\delta^{34}S(\Sigma S)$ estimation is given in Appendix A.

Lead isotopes provide additional constraints on the source of metals in ore deposits. The Pb isotope data of the syn-ore stage minerals from V8, V1 and V11 orebodies were plotted in Fig. 7. In the $^{206}Pb/^{204}Pb$ versus $^{207}Pb/^{204}Pb$ diagram and $^{206}Pb/^{204}Pb$ versus $^{208}Pb/^{204}Pb$ diagrams, all the data were projected toward around mantle evolution lines and extended to the upper and lower crust evolution lines, implying the Pb sourece from mixing of lower and upper crust or mental. Besides, the Pb isotope data of the feldspar of Duerji granite, muscovite granite, biotite granite and diorite dyke in mine area also plotted in Fig. 7 (Zhu et al., 2006). Obviously, lead isotopic compositions of the Meng'entaolegai sulphides are consistent with those of the diorite dyke, indicating that the diorite contributed to ore-forming materials.

6 CONCLUSIONS

(1) The Meng'entaolegai deposit formed in an H_2O-NaCl magmatic hydrothermal system with medium temperature and medium salinity. The syn-ore stage in the western and middle ore-blocks was resulted from fluid boiling. However, the syn-ore stage ore-forming fluids in the eastern ore-block were likely formed mainly by the mixing of magmatic fluid with meteoric fluid, based on FI and H-O isotope data.

(2) The sulfur source was magmatic and Pb was sourced from mixing of lower and upper crust for the syn-ore stage in all the ore-blocks.

(3) Thermodynamic modelling shows that the fluid conditions of the syn-ore stage in the western and middle ore-blocks were very similar and showed high f_{O_2}, low pH and low S, but those in the eastern ore-block may have changed into low f_{O_2}, high pH and high Total S.

(4) Thermodynamic modelling also shows that from the middle to the eastern ore-blocks, the Ag activity dropped from 10^{-9} to 10^{-12}. We attribute this to pH change caused by fluid mixing. Thus, meteoric water incursion likely played a significant role in Ag mineralization in the eastern ore-block, and explains why Ag was mainly precipitated in the eastern ore-block.

ACKNOWLEDGMENTS

We thank Prof. Guoxiang Chi, Prof. Hongrui Fan and anonymous reviewers for their constructive comments that helped to improve the manuscript. We are grateful to the staff of the Analytical Laboratory in Beijing Research Institute of Uranium Geology, China National Nuclear Corporation (CNNC) for their advice and assistance in the isotope analysis. This work was financially supported by the Open Foundation of Key Laboratory of Mineral Resources Evaluation in Northeast Asia, and the Ministry of Natural Resources of China. The final publication is available at Springer via https://doi.org/10.1007/s12583-019-1273-2.

Electronic Supplementary Material: Supplementary material (Appendix A) is available in the online version of this article at https://doi.org/10.1007/s12583-019-1273-2.

REFERENCES CITED

Chen, Y. J., Chen, H. Y., Zaw, K., et al., 2007. Geodynamic Settings and Tectonic Model of Skarn Gold Deposits in China: An Overview. *Ore Geology Reviews*, 31(1/2/3/4): 139–169. https://doi.org/10.1016/j.oregeorev.2005.01.001

Chi, G. X., Haid, T., Quirt, D., et al., 2016. Petrography, Fluid Inclusion Analysis, and Geochronology of the End Uranium Deposit, Kiggavik, Nunavut, Canada. *Mineralium Deposita*, 52(2): 211–232. https://doi.org/10.1007/s00126-016-0657-9

Chi, G. X., Lu, H. Z., 2008. Validation and Representation of Fluid Inclusion Microthermometric Data Using the Fluid Inclusion Assemblage (FIA) Concept. *Acta Petrologica Sinica*, 24 (9): 1945–1953

Clayton, R. N., Mayeda, T. K., 1963. The Use of Bromine Pentafluoride in the Extraction of Oxygen from Oxides and Silicates for Isotopic Analysis. *Geochimica et Cosmochimica Acta*, 27(1): 43–52. https://doi.org/10.1016/0016-7037(63)90071-1

Driesner, T., Heinrich, C. A., 2007. The System H_2O-NaCl. Part I: Correlation Formulae for Phase Relations in Temperature-Pressure-Composition Space from 0 to 1 000 °C, 0 to 5 000 bar, and 0 to 1 XNaCl. *Geochimica et Cosmochimica Acta*, 71(20): 4880–4901. https://doi.org/10.1016/j.gca.2006.01.033

Fan, H. R., Hu, F. F., Wilde, S. A., et al., 2011. The Qiyugou Gold-Bearing Breccia Pipes, Xiong'ershan Region, Central China: Fluid-Inclusion and Stable-Isotope Evidence for an Origin from Magmatic Fluids. *International Geology Review*, 53(1): 25–45. https://doi.org/10.1080/00206810902875370

Giggenbach, W. F., 1982. Geochemistry of Hydrothermal Ore Deposits, 2nd Edition. *Geochimica et Cosmochimica Acta*, 46(5): 833. https://doi.org/10.1016/0016-7037(82)90034-5

Goldstein, R. H., 2001. Fluid Inclusions in Sedimentary and Diagenetic Systems. *Lithos*, 55(1/2/3/4): 159–193. https://doi.org/10.1016/s0024-4937(00)00044-x

Greg, M. A., David, A. C., 1993. Thermodynamics in Geochemistry: The Equilibrium Model. Oxford University Press, Oxford. 1189

Hedenquist, J. W., Henley, R. W., 1985. The Importance of CO_2 on Freezing Point Measurements of Fluid Inclusions; Evidence from Active Geothermal Systems and Implications for Epithermal Ore Deposition. *Economic Geology*, 80(5): 1379–1406. https://doi.org/10.2113/gsecongeo.80.5.1379

Helgeson, H. C., Kirkham, D. H., 1974. Theoretical Prediction of the Thermodynamic Behavior of Aqueous Electrolytes at High Pressures and Temperatures; II, Debye-Huckel Parameters for Activity Coefficients and Relative Partial Molal Properties. *American Journal of Science*, 274(10): 1199–1261. https://doi.org/10.2475/ajs.274.10.1199

Hennet, R. J. C., Crerar, D. A., Schwartz, J., 1988. Organic Complexes in Hydrothermal Systems. *Economy Geology*, 83(4): 742–764

Hollister, L. S., Burruss, R. C., 1976. Phase Equilibria in Fluid Inclusions from the Khtada Lake Metamorphic Complex. *Geochimica et Cosmochimica Acta*, 40(2): 163–175. https://doi.org/10.1016/0016-7037(76)90174-5

Jahn, B. M., 2004. The Central Asian Orogenic Belt and Growth of the Continental Crust in the Phanerozoic. In: Malpas, J., Fletcher, C. J. N., Ali, J. R., et al., eds., Aspects of the Tectonic Evolution of China. *Special Publication 226*, 73–100

Jiang, S. H., Nie, F. J., Liu, Y. F., et al., 2011. Geochronology of Intrusive

Rocks Occurring in and around the Mengentaolegai Silver-Polymetallic Deposit, Inner Mongolia. *Journal of Jilin University* (*Earth Science Edition*), 46(6): 1755–1769

Johnson, J. W., Oelkers, E. H., Helgeson, H. C., 1992. SUPCRT92: A Software Package for Calculating the Standard Molal Thermodynamic Properties of Minerals, Gases, Aqueous Species, and Reactions from 1 to 5 000 Bar and 0 to 1 000 °C. *Computers & Geosciences*, 18(7): 899–947. https://doi.org/10.1016/0098-3004(92)90029-q

Kissin, S. A., Mango, H., 2014. Silver Vein Deposits. Treatise on Geochemistry, Elsevier, Oxford. 425–432

Klemm, L. M., Pettke, T., Heinrich, C. A., et al., 2007. Hydrothermal Evolution of the El Teniente Deposit, Chile: Porphyry Cu-Mo Ore Deposition from Low-Salinity Magmatic Fluids. *Economic Geology*, 102(6): 1021–1045. https://doi.org/10.2113/gsecongeo.102.6.1021

Li, X. M., Li, Z. K., Xiong, S. K., et al., 2019. Mineralization Characteristics of the Laoliwan Ag-Pb-Zn Deposit and Geochemical Features of the Ore-Bearing Granite Porphyry in the Southern North China Craton: Implications for Ore Genesis. *Earth Science*, 44(1): 69–87. https://doi.org/10.3799/dqkx.2018.147 (in Chinese with English Abstract)

Liu, C. H., Bagas, L., Wang, F. X., 2016. Isotopic Analysis of the Super-Large Shuangjianzishan Pb-Zn-Ag Deposit in Inner Mongolia, China: Constraints on Magmatism, Metallogenesis, and Tectonic Setting. *Ore Geology Reviews*, 75: 252–267. https://doi.org/10.1016/j.oregeorev.2015.12.019

Liu, Y. F., Jiang, S. H., Bagas, L., 2016. The Genesis of Metal Zonation in the Weilasituo and Bairendaba Ag-Zn-Pb-Cu-(Sn-W) Deposits in the Shallow Part of a Porphyry Sn-W-Rb System, Inner Mongolia, China. *Ore Geology Reviews*, 75: 150–173. https://doi.org/10.1016/j.oregeorev.2015.12.006

Maanijou, M., Rasa, I., Lentz, D. R., 2012. Petrology, Geochemistry, and Stable Isotope Studies of the Chehelkureh Cu-Zn-Pb Deposit, Zahedan, Iran. *Economic Geology*, 107(4): 683–712. https://doi.org/10.2113/econgeo.107.4.683

Mao, J. W., Xie, G. Q., Zhang, Z. H., et al., 2005. Mesozoic Large-Scale Metallogenic Pluses in North China and Corresponding Geodynamic Settings. *Acta Petrolei Sinica*, 21: 169–188 (in Chinese with English Abstract)

Ohmoto, H., 1972. Systematics of Sulfur and Carbon Isotopes in Hydrothermal Ore Deposits. *Economic Geology*, 67(5): 551–578. https://doi.org/10.2113/gsecongeo.67.5.551

Ohmoto, H., Goldhaber, M. B., 1997. Sulfur and Carbon Isotopes. In: Barnes, H. L., ed., Geochemistry of Hydrothermal Ore Deposits, Wiley, New York. 517–611

Ouyang, H. G., Mao, J. W., Santosh, M., et al., 2014. The Early Cretaceous Weilasituo Zn-Cu-Ag Vein Deposit in the Southern Great Xing'an Range, Northeast China: Fluid Inclusions, H, O, S, Pb Isotope Geochemistry and Genetic Implications. *Ore Geology Reviews*, 56: 503–515. https://doi.org/10.1016/j.oregeorev.2013.06.015

Qi, J. P., Chen, Y. J., Pirajno, F., 2005. Geological Characteristics and Tectonic Setting of the Epithermal Deposits in the Northeast China. *Journal of Mineralogy & Petrology*, 25: 47–59

Robinson, B. W., Kusakabe, M., 1975. Quantitative Preparation of Sulfur Dioxide, for Sulfur-34/Sulfur-32 Analyses, from Sulfides by Combustion with Cuprous Oxide. *Analytical Chemistry*, 47(7): 1179–1181. https://doi.org/10.1021/ac60357a026

Robinson, B. W., Ohmoto, H., 1973. Mineralogy, Fluid Inclusions, and Stable Isotopes of the Echo Bay U-Ni-Ag-Cu Deposits, Northwest Territories, Canada. *Economic Geology*, 68(5): 635–656. https://doi.org/10.2113/gsecongeo.68.5.635

Roedder, E., 1984, Fluid Inclusions. In: Ribbe, P. H., ed., Reviews in Mineralogy. Mineralogical Society of America, Chantilly. 644

Ruan, B. X., Lü, X. B., Yang, W., et al., 2015. Geology, Geochemistry and Fluid Inclusions of the Bianjiadayuan Pb-Zn-Ag Deposit, Inner Mongolia, NE China: Implications for Tectonic Setting and Metallogeny. *Ore Geology Reviews*, 71: 121–137. https://doi.org/10.1016/j.oregeorev.2015.05.004

Shu, Q. H., Chang, Z. S., Lai, Y., et al., 2016. Regional Metallogeny of Mo-Bearing Deposits in Northeastern China, with New Re-Os Dates of Porphyry Mo Deposits in the Northern Xilamulun District. *Economic Geology*, 111(7): 1783–1798. https://doi.org/10.2113/econgeo.111.7.1783

Shu, Q., Lai, Y., Sun, Y., et al., 2013. Ore Genesis and Hydrothermal Evolution of the Baiyinnuo'er Zinc-Lead Skarn Deposit, Northeast China: Evidence from Isotopes (S, Pb) and Fluid Inclusions. *Economic Geology*, 108(4): 835–860. https://doi.org/10.2113/econgeo.108.4.835

Skirrow, R. G., Walshe, J. L., 2002. Reduced and Oxidized Au-Cu-Bi Iron Oxide Deposits of the Tennant Creek Inlier, Australia: An Integrated Geologic and Chemical Model. *Economic Geology*, 97(6): 1167–1202. https://doi.org/10.2113/gsecongeo.97.6.1167

Steele-MacInnis, M., Lecumberri-Sanchez, P., Bodnar, R. J., 2012. HOKIEFLINCS_H_2O-NACL: A Microsoft Excel Spreadsheet for Interpreting Microthermometric Data from Fluid Inclusions Based on the PVTX Properties of H_2O-NaCl. *Computers & Geosciences* 49 (*Complete*), 334–337

Su, W. C., Hu, R. Z., Qi, L., et al., 2001. Trace Elements in Fluid Inclusions in the Carlin-Type Gold Deposits, Southwestern Guizhou Province. *Chinese Journal of Geochemistry*, 20(3): 233–239. https://doi.org/10.1007/bf03166144

Taylor, H. P. Jr, 1974. The Application of Oxygen and Hydrogen Isotope Studies to Problem of Hydrothermal Alteration and Ore Deposition. *Economic Geology*, 69(6): 843–883

Wang, Z. G., Wang, K. Y., Wan, D., et al., 2017. Metallogenic Age and Hydrothermal Evolution of the Jidetun Mo Deposit in Central Jilin Province, Northeast China: Evidence from Fluid Inclusions, Isotope Systematics, and Geochronology. *Ore Geology Reviews*, 89: 731–751. https://doi.org/10.1016/j.oregeorev.2017.07.014

Wilde, S. A., Zhou, J. B., 2015. The Late Paleozoic to Mesozoic Evolution of the Eastern Margin of the Central Asian Orogenic Belt in China. *Journal of Asian Earth Sciences*, 113: 909–921. https://doi.org/10.1016/j.jseaes.2015.05.005

Wilkinson, J. J., 2001. Fluid Inclusions in Hydrothermal Ore Deposits. *Lithos*, 55(1/2/3/4): 229–272. https://doi.org/10.1016/s0024-4937(00)00047-5

Wu, H. Y., Zhang, L. C., Wan, B., et al., 2011a. Re-Os and $^{40}Ar/^{39}Ar$ Ages of the Jiguanshan Porphyry Mo Deposit, Xilamulun Metallogenic Belt, NE China, and Constraints on Mineralization Events. *Mineralium Deposita*, 46(2): 171–185. https://doi.org/10.1007/s00126-010-0320-9

Wu, H. Y., Zhang, L. C., Wan, B., et al., 2011b. Geochronological and Geochemical Constraints on Aolunhua Porphyry Mo-Cu Deposit, Northeast China, and Its Tectonic Significance. *Ore Geology Reviews*, 43(1): 78–91. https://doi.org/10.1016/j.oregeorev.2011.07.007

Zartman, R. E., Doe, B. R., 1981. Plumbotectonics—The Model. *Tectonophysics*, 75(1/2): 135–162. https://doi.org/10.1016/0040-1951(81)90213-4

Zeng, Q. D., Liu, J. M., Zhang, Z. L., et al., 2009. Geology and Lead-Isotope Study of the Baiyinnuoer Zn-Pb-Ag Deposit, South Segment of the Da Hinggan Mountains, Northeastern China. *Resource Geology*, 59(2):

170–180. https://doi.org/10.1111/j.1751-3928.2009.00088.x

Zeng, Q. D., Liu, J. M., Zhang, Z. L., et al., 2011. Geology and Geochronology of the Xilamulun Molybdenum Metallogenic Belt in Eastern Inner Mongolia, China. *International Journal of Earth Sciences*, 100(8): 1791–1809. https://doi.org/10.1007/s00531-010-0617-z

Zhai, D. G., Liu, J. J., 2014. Gold-Telluride-Sulfide Association in the Sandaowanzi Epithermal Au-Ag-Te Deposit, NE China: Implications for Phase Equilibrium and Physicochemical Conditions. *Mineralogy and Petrology*, 108(6): 853–871. https://doi.org/10.1007/s00710-014-0334-6

Zhai, D. G., Liu, J. J., Cook, N. J., et al., 2018. Mineralogical, Textural, Sulfur and Lead Isotope Constraints on the Origin of Ag-Pb-Zn Mineralization at Bianjiadayuan, Inner Mongolia, NE China. *Mineralium Deposita*, 54(1): 47–66. https://doi.org/10.1007/s00126-018-0804-6

Zhai, D. G., Liu, J. J., Wang, J. P., et al., 2013. Fluid Evolution of the Jiawula Ag-Pb-Zn Deposit, Inner Mongolia: Mineralogical, Fluid Inclusion, and Stable Isotopic Evidence. *International Geology Review*, 55(2): 204–224. https://doi.org/10.1080/00206814.2012.692905

Zhai, D. G., Liu, J. J., Wang, J. P., et al., 2014a. Zircon U-Pb and Molybdenite Re-Os Geochronology, and Whole-Rock Geochemistry of the Hashitu Molybdenum Deposit and Host Granitoids, Inner Mongolia, NE China. *Journal of Asian Earth Sciences*, 79: 144–160. https://doi.org/10.1016/j.jseaes.2013.09.008

Zhai, D. G., Liu, J. J., Zhang, H. Y., et al., 2014b. Origin of Oscillatory Zoned Garnets from the Xieertala F-Zn Skarn Deposit, Northern China: *In-situ* LA-ICP-MS Evidence. *Lithos*, 190–191: 279–291. https://doi.org/10.1016/j.lithos.2013.12.017

Zhai, D. G., Liu, J. J., Zhang, H. Y., et al., 2014c. S-Pb Isotopic Geochemistry, U-Pb and Re-Os Geochronology of the Huanggangliang Fe-Sn Deposit, Inner Mongolia, NE China. *Ore Geology Reviews*, 59: 109–122. https://doi.org/10.1016/j.oregeorev.2013.12.005

Zhang, Q., Zhan, X. Z., Liu, Z. H., et al., 2004. Trace Element Geochemistry of Meng'entaolegai Ag-Pb-Zn-In Deposit, Inner Mongolia, China. *Acta Mineralogica Sinica*, 24(1): 39–47

Zhang, Q., Zhu, X. Q., He, Y. L., et al., 2006. Indium Enrichment in the Meng'entaolegai Ag-Pb-Zn Deposit, Inner Mongolia, China. *Resource Geology*, 56(3): 337–346. https://doi.org/10.1111/j.1751-3928.2006.tb00287.x

Zhao, Y. M., Zhang, D. Q., 1997. Metallogeny and Prospective Evaluation of Copper-Polymetallic Deposits in the Da Hinggan Mountains and Its Adjacent Regions. Seismological Press, Beijing. 83–106 (in Chinese with English Abstract)

Zhu, J. J., Hu, R., Richards, J. P., et al., 2015. Genesis and Magmatic-Hydrothermal Evolution of the Yangla Skarn Cu Deposit, Southwest China. *Economic Geology*, 110(3): 631–652. https://doi.org/10.2113/econgeo.110.3.631

Zhu, X. Q., Zhang, Q., He, Y. L., et al., 2006. Hydrothermal Source Rocks of the Meng'entaolegai Ag-Pb-Zn Deposit in the Granite Batholith, Inner Mongolia, China: Constrained by Isotopic Geochemistry. *Geochemical Journal*, 40(3): 265–275. https://doi.org/10.2343/geochemj.40.265